Enabling Ultraviolet Lasers for Touchless Spacecraft Potential Sensing

Álvaro Romero-Calvo, Kaylee Champion, and Hanspeter Schaub

***Abstract*— Ultraviolet (UV) lasers are proposed as a replacement for low-energy electron beams in touchless spacecraft potential sensing. Theoretical considerations support their use as photoelectron sources due to their insensitivity to the electrostatic environment, which leads to more robust and controllable systems. The feasibility of this approach is verified in a representative scenario of application, and its relevance for spacecraft charge control and material identification is discussed. A simplified photoemission framework is presented and validated with vacuum chamber experiments by means of particle tracing simulations, showing that such a framework can be used to determine the spatial distribution of photoelectrons emanating from a target surface and an informed estimate of its magnitude. The possibility of combining this method with high-energy electron beams is also discussed as a way to enhance the robustness and accuracy of the sensing process. Ultimately, the analysis supports the use of UV lasers in a wide range of spacecraft charging technologies in geosynchronous orbit and deep space.**

***Index Terms*— Particle tracing, photoelectric effect, spacecraft charging, space weather.**

I. Introduction

THE sustainable long-term exploration, development, and utilization of the cislunar space is one of NASA's strategic goals and a necessary preliminary step for Mars missions [1]. Spacecraft charging represents a major challenge in these environments, where low-density high-temperature plasma can lead to significant charging events [2]. The problem shares some characteristics with previous experiences at the geosynchronous equatorial orbit (GEO), where spacecraft have been shown to charge up to tens of kilovolts depending on local space weather conditions [3].

To compensate for and, eventually, exploit spacecraft charging beyond low-earth orbit (LEO), novel active sensing methods are currently under development to touchlessly sense the electrostatic potential of non-cooperative objects in GEO and deep space. Such approaches make use of a positively charged servicing craft that directs an electron beam at the object of interest 10–30 m from the servicer so that low-energy secondary electrons [4], [5] and X-rays [6], [7] are emitted from its surface. The positively charged servicer attracts electron emissions that are detectable compared with the ambient environment [8], [9], characterizes the incoming fluxes, and, knowing its own potential, infers that of the target. This information can be used to compensate for electrostatic perturbations in close-proximity multi-spacecraft operations [10], [11], minimize the risk of electrostatic discharge during rendezvous, control spacecraft formations [12], and detumble [13] or reorbit [14], [15], [16], [17], [18] space debris by means of electrostatic forces, among others.

Moderate electron beam energies are preferred in the secondary electron method to maximize the secondary electron yield, which generally decays for energetic impacts [2]. However, that makes particle dynamics particularly susceptible to the inhomogeneous electrostatic environment generated by the servicer–target system, increasing the uncertainty of the problem [5], [19]. Modeling is also undermined by the degradation of surface materials, which occurs after a prolonged exposition to the GEO environment [20]. Even the slightest change in surface conditions can alter surface properties [21], [22], [23], [24], [25], which are usually obtained in a controlled laboratory environment. This adds a layer of complexity that must be accounted for while sensing. From a technical perspective, it would be convenient to develop a sensing method that overcomes these challenges. Analytical and experimental studies have also shown that the combined measurement of secondary electrons and X-rays enhances the robustness and accuracy of the target potential sensing process [19], [26]. However, the physics of each problem is not favorable to the simultaneous generation of both the signals because the generation of X-rays is favored by energetic electron beams [6], [27]. Uncoupling both the mechanisms to optimize the generation and control of secondary electrons and X-rays is, therefore, desirable.

The use of ultraviolet (UV) lasers is proposed in this work to excite the emission of photoelectrons in non-cooperative GEO objects as conceptualized in Fig. 1. From a more general perspective, high-energy electron beams could also be used to simultaneously induce X-ray generation. Major sources of uncertainty are eliminated with this approach due to: 1) the independence of UV photons from the complex electrostatic environment; 2) the high directivity of quasi-relativistic

Manuscript received 22 August 2022; revised 12 March 2023; accepted 3 April 2023. Date of publication 21 April 2023; date of current version 12 October 2023. This work was supported in part by the U.S. Air Force Office of Scientific Research under Grant FA9550-20-1-0025 and in part by the Rafael del Pino Foundation under its 2021 Excellence Fellowship. The review of this article was arranged by Senior Editor S. T. Lai. *(Corresponding author: Álvaro Romero-Calvo.)*

Álvaro Romero-Calvo is with the Daniel Guggenheim School of Aerospace Engineering, Georgia Institute of Technology, Atlanta, GA 30332 USA (e-mail: alvaro.romerocalvo@gatech.edu).

Kaylee Champion and Hanspeter Schaub are with the Smead Aerospace Engineering Sciences Department, University of Colorado at Boulder, Boulder, CO 80309 USA (e-mail: Kaylee.Champion@colorado.edu; Hanspeter.Schaub@colorado.edu).

Color versions of one or more figures in this article are available at https://doi.org/10.1109/TPS.2023.3264914.

Digital Object Identifier 10.1109/TPS.2023.3264914

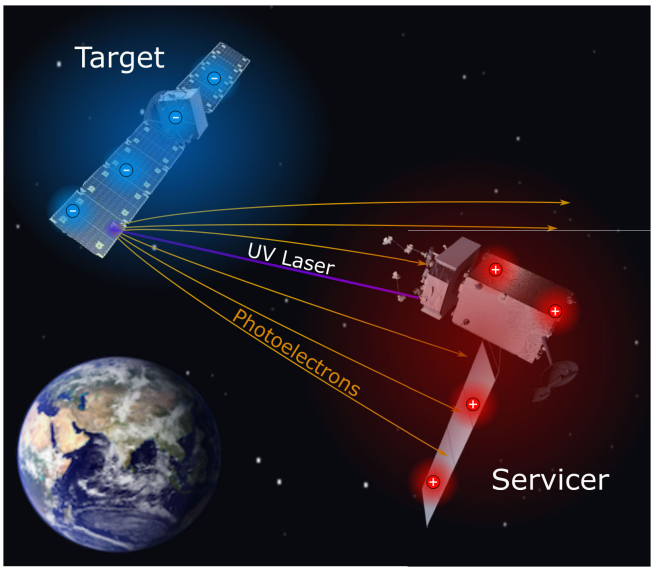

Fig. 1. Conceptual representation of the photoelectron generation process.

electron beams; and 3) the relative stability of surface properties with surface contamination for energetic photon and electron impacts. The successful development of spaceborne UV lasers could therefore overcome previous sensing methods, but this approach remains largely unexplored.

The main goals of this work are to assess the feasibility of using UV lasers for touchless potential sensing and identify the main challenges of this approach. A third goal is to unveil applications where UV sources, either alone or in combination with electron beams, can have a positive impact. The theoretical, numerical, and experimental methods used in this work are discussed in Section II. The results are derived in Section III and used in Section IV to discuss the prospects, challenges, and feasibility of several UV touchless potential control and sensing applications.

II. Materials and Methods

The numerical and experimental tools adopted in this article complement those introduced in [5], where a detailed discussion of the secondary electron processes and related particle tracing simulations is provided. For the sake of compactness, only aspects of direct relevance to this article are subsequently discussed.

A. Photoelectron Emission

In addition to fundamental spacecraft charging processes, an excellent review of which can be found in [2], the touchless spacecraft potential sensing methods discussed in this work rely on the emission of secondary and backscattered electrons, photoelectrons, and X-rays. An overview of the secondary electron [5], [28], [29], backscattered electron [5], [30], and X-rays [6], [31], [32], [33] emission processes may be found in previous works and are complemented with the photoelectron emissions analysis provided in this section.

The probability of emission of a photoelectron per photon collision is determined by the photoelectric yield [2]

$$Y[\omega, \phi, R] = Y^*[\omega, \phi][1 - R] \tag{1}$$

where $Y^*[\omega, \phi]$ is the yield per absorbed photon, ω is the photon energy (related to the wavelength λ through $\omega = hc/\lambda$, with h being Planck's constant), ϕ is in this case the photon incidence angle, and $R(\omega, \phi, \sigma)$ is the surface reflectance, which depends on the photon energy, incidence angle, and root mean square surface roughness σ. The incidence angle effect on the yield is, in first-order approximation and for $\cos\phi > 0.1$ [34],

$$Y^*[\omega, \phi] \approx \frac{Y^*[\omega, 0]}{\cos\phi} \tag{2}$$

but since $1 - R(\omega, \phi, \sigma)$ also has the approximate dependence [35], [36]

$$1 - R(\omega, \phi, \sigma) \approx [1 - R(\omega, 0, \sigma)]\cos\phi \tag{3}$$

both $\cos\phi$ terms cancel in (1). Therefore, $Y[\omega, R]$ is not, in first-order approximation, a function of the photon incidence angle [2]. As discussed in Section III, this assumption is not appropriate for high incidence angles.

The total reflectance is expressed as the sum of specular (R_s) and diffuse (R_d) reflectances

$$R(\omega, 0, \sigma) = R_s(\omega, 0, \sigma) + R_d(\omega, 0, \sigma) \tag{4}$$

which are defined as

$$R_s(\omega, 0, \sigma) = R_0(\omega)\exp\left[\frac{-(4\pi\sigma)^2}{\lambda^2}\right] \tag{5}$$

$$R_d(\omega, 0, \sigma) = R_0(\omega)\frac{(4\pi\sigma)^2}{\lambda^2} \tag{6}$$

with $R_0(\omega)$ being the normal reflectance of a perfectly smooth surface of the impacted material, $\lambda = hc/\omega$ the photon wavelength, h Planck's constant, and c the speed of light [37]. The ratio of diffuse to specular reflectances is

$$\frac{R_d}{R_s} = \frac{(4\pi\sigma)^2}{\lambda^2}\exp\left[\frac{(4\pi\sigma)^2}{\lambda^2}\right] \tag{7}$$

implying that for small wavelength and large surface roughness the diffuse term is the major contributor to the total reflectance. Reflected photons experience negligible energy variations [36] and generate photoelectrons at different surfaces.

The trajectory of electrons excited by photons is assumed to resemble the propagation of secondary electrons out of a surface material. Thus, photoelectrons' angular emission distribution is approximated with Lambert's cosine law and is nearly independent of the angle of incidence of the impinging particle [38]. At the particle level, the polar angle can be computed from a uniform 0–1 random variable x through [39]

$$\theta = \frac{1}{2}\text{acos}(1 - 2x) \tag{8}$$

while the azimuth angle follows a uniform distribution between 0° and 360°. The photoelectron maximum emission energy follows the relation

$$E_{p,\max} = \omega - \varphi \tag{9}$$

where φ is the work function of the material. The Ly-α line (121.6 nm, 10.2 eV) is dominant in the solar spectrum,

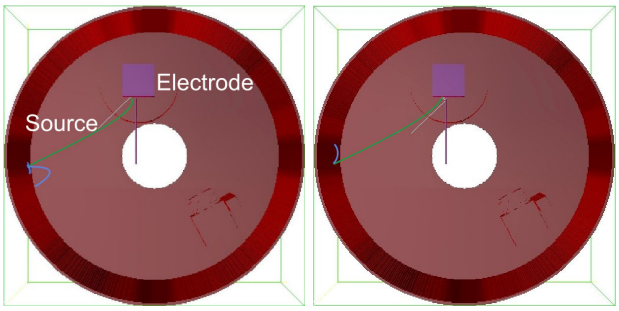

(a) (b)

Fig. 2. SIMION examples of photons (white) being generated and reflected, leading to the emission of photoelectrons (green) and secondary electrons (blue) inside the ECLIPS vacuum chamber. (a) Immediate photon absorption. (b) Photon reflection and absorption.

and hence the photoelectron energy will reach a theoretical maximum of 5–6 eV after accounting for a work function of 4–5 eV. Because photoelectrons have to propagate through the material, their emission energy distribution is usually centered around 1–3 eV [36]. Therefore, a small positive spacecraft potential will act as a potential well and attract photoelectrons back to the surface [40].

B. Particle Tracing Framework

A necessary preliminary step for the use of active photoemission in potential sensing applications is the development of suitable numerical simulation frameworks. A similar need motivates in [5] the development and validation of a SIMION particle tracing model for the secondary-electron-based sensing problem. What follows is an extension of such model that considers photons, photoelectrons, and secondary electrons resulting from the impact of the latter on the electrode surfaces.

1) Implementation: The particle tracing model adopts the electrostatic framework introduced in Appendix A and the technical approximations to photoelectron emission presented in Section II-A. Given that the model has already been thoroughly described in [5], what follows is a description of the implementation of the photoelectric effect in SIMION, achieved with user-defined LUA functions.

Photons are modeled as particles with zero charge and arbitrary mass and speed that, follow rectilinear trajectories. The impact of a photon on a charged surface triggers the application of (3) to determine whether it is reflected or not. If the photon is absorbed into the material, photoelectrons may be generated based on the photoelectric yield in (2). A Poisson point process is used to compute the probability of emission. Lambert's cosine law, described by (8), is considered for the angular distribution of emitted photoelectrons, which are released with fixed initial energy. Photoelectrons that impact a second surface may generate secondary electrons following the procedures described in [5]. The normal incidence parameters $R_0(\omega)$ and $Y^*(\omega, 0)$ and the work function φ are taken as external inputs.

Reflected photons keep flying under specular or diffuse schemes, depending on the ratio given by (7). Specular reflections are trivial to implement in SIMION, while diffuse reflections are modeled following Lambert's cosine law in (8). A maximum number of successive reflections can be imposed for computational efficiency. An overview of the new processes implemented in the model is given in Fig. 2 for a single emitted photon and the experimental setup described in Section II-C.

2) Effective Values: The photoelectric yield $Y^*(\omega, 0)$ and maximum initial photoelectron energy $E_{p,\max}(\omega)$ depend on the energy ω of the incident photon. However, photons are implemented as particles with arbitrary mass and speed, so they do not contain any spectral information. Although this would certainly be easy to correct in SIMION, a simpler and more computationally efficient approach is adopted in this work.

Knowing the normalized spectrum $S(\omega)$ of the UV source, the *effective* photoelectric yield

$$Y^*_{\text{eff}}(0) = \int_0^\infty Y^*(\omega, 0) S(\omega) d\omega \tag{10}$$

can be computed as the average number of photoelectrons released per impinging photon. This value faithfully reproduces the response of the system due to the large number of photons involved. In addition, the mean photoelectron energy

$$\overline{E}_p = \int_\varphi^\infty \omega S(\omega) d\omega - \varphi \tag{11}$$

is adopted for each photoelectron released in SIMION assuming no energy loss. This simplification is appropriate because initial photoelectron energies are of the order of few eVs, but since the electrostatic environment is dominated by large spacecraft potentials, small variations in this value have a negligible effect in the overall flux. In the space environment, the emission energy could be reasonably approximated as 1–3 eV [36].

3) Superparticle Method: The photoelectric yield is of the order of 10^{-7} electrons per photon for most materials and low photon energies, as shown in Appendix B, meaning that a large number of photons have to be simulated in SIMION to release a single photoelectron. To overcome this computational issue, the effective photoelectric yield computed in (10) is multiplied by a scale factor κ to accelerate the simulation, leading to the *virtual* photoelectric yield

$$Y^*_{\text{virt}}(0) = \kappa Y^*_{\text{eff}}(0). \tag{12}$$

Each photon is thus treated as a *superphoton* that represents κ particles. As a consequence, the current measured by the RPA as predicted by the simulation needs to be adjusted accordingly. The number of photons coming out of the UV source per second is

$$n_{\text{ph}} = \frac{P_{\text{ph}}}{\overline{\omega}} \tag{13}$$

where P_{ph} is the output power of the source and $\overline{\omega}$ is the average photon energy, computed as

$$\overline{\omega} = \int_0^\infty \omega S(\omega) d\omega. \tag{14}$$

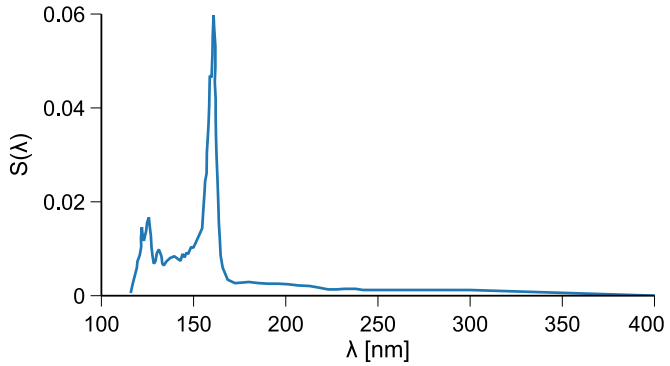

Fig. 3. Normalized spectrum of the Hamamatsu L10706-S2D2 UV light source [41].

If n_{sim} photons are simulated with a scale factor κ and a number $n_{e\text{-,det}}$ of electrons enter the detector during the simulation, then the actual measured current is

$$I_{\text{det}} = \eta_{\text{det}} \frac{n_{\text{ph}}}{\kappa n_{\text{sim}}} q_e n_{e\text{-,det}} \tag{15}$$

with η_{det} being the efficiency of the detector.

4) Configuration: The SIMION model is configured with the material properties listed in Appendix B. The values $E_{\max} \approx 300$ eV, $\delta_{\max} \approx 0.97$ [2], and $\varphi \approx 4$ eV [42] are adopted for the aluminum targets to simulate secondary electron emission. The reflectivity R_0 of aluminum is assumed to be 0.9, while that of the steel walls of the chamber is limited to 0.1. In all, 2 00 000 photons are simulated for the computation of the numerical results presented in Section III.

The average photon energy resulting from the Hamamatsu L10706-S2D2 UV light spectrum in Fig. 3 is $\overline{E}_p \approx 4$ eV, while the effective photoelectron yield becomes $Y^*_{\text{eff}}(0) \approx 5.88 \cdot 10^{-2}$ assuming the ideal photoelectric yield shown in Appendix B and C and Fig. 13 [43]. A scale factor $\kappa = 10$ is adopted, which returns a virtual yield $Y^*_{\text{virt}}(0) \approx 5.88 \cdot 10^{-1}$. Private communication with the manufacturer has revealed that the power P_{ph} emitted by the lamp is approximately 1.2 mW, which corresponds to a 160-nm irradiance peak of 0.14 μWcm^{-2}nm^{-1} at 50 cm from the source.

Once again, it is important to highlight that surface conditions can have a very significant impact on these values [20], [21], [22], [23], which should be taken as a rough estimate. In the case of aluminum, used to validate the numerical framework in Section III, the generation of a thin oxide layer is the main source of uncertainty. Further work is necessary to quantify how the formation of an oxide layer impacts the efficiency of photoelectron emissions for this and other applications. However, as shown in Figs. 13 and 14, as the photon energy increases, the photoelectron yield and reflectance converge to comparable values for several materials. Similar to other electron surface processes [44], this may be interpreted as a consequence of the deeper penetration of photons into the material, which makes surface-related effects less relevant from a technical perspective. Minimizing the wavelength of the UV laser is therefore advisable to reduce material-related uncertainties.

5) Calibration: The geometrical parameters of the particle tracing model have to be adjusted to ensure an accurate representation of the physical system. Fig. 4 shows comparison of the experimental setup with the SIMION model for different rotation angles. The electrode assembly is illuminated by the UV light while the panel is covered by a sheet of paper that eases visualization. The model and electrode assembly depict the same illuminated area, which is indicative of a successful calibration of the UV light. However, the UV lamp illuminates areas outside the central bright spot and generates a complex radial distribution. This is a source of uncertainty that cannot be easily accounted for without dedicated characterization equipment. Focused UV lasers or limited aperture could potentially be used in future applications to mitigate this effect. However, the purpose of the experiments is to validate the theoretical model, as described in Section III-B, and this is achieved without the need to compensate for this second-order effect.

6) Space-Charge Effects: In the presence of charged spacecraft, the surrounding plasma tends to relocate under the influence of the perturbed electrostatic field following a process known as Debye screening [45]. For a sphere with radius R_{SC} and low surface potential V_{SC} ($\ll k_B T_e/q_e$), the electrostatic potential field is damped under the Debye-HC<ckel approximation [46]

$$V(r) = -\frac{V_{\text{SC}} R_{\text{SC}}}{r} e^{-\frac{r-R_{\text{SC}}}{\lambda_D}} \tag{16}$$

where

$$\lambda_D = \sqrt{\frac{\epsilon_0 k_B T_e}{n_e q_e^2}} \tag{17}$$

is a characteristic distance known as the Debye length, r is the radial coordinate, k_B is Boltzmann's constant, T_e is the electron temperature, n_e is the electron density, and q_e is the elementary charge. The radial electric field is computed with (33) from (16), becoming

$$E(r) = \frac{V_{\text{SC}} R_{\text{SC}}}{r^2} e^{-\frac{r-R_{\text{SC}}}{\lambda_D}} \left(1 + \frac{r}{\lambda_D}\right). \tag{18}$$

The nominal value of λ_D in GEO is ~200 m [46], implying that the exponential terms in (16) and (18) have a second-order effect on the electron detection process for distances of the order of tens of meters. In addition, the geomagnetic field in GEO orbit is 100 nT, resulting in gyroradii of 100–3000 m for electron energies from 10 to 10^4 eV [5]. This is several times larger than the separation distance of 30 m and is considered a secondary effect compared with the electrostatic field for this study. In other words, the unperturbed electrostatic potential obtained by solving (34) offers a good approximation of the actual electrostatic environment while minimizing the computational costs.

Even though overall space charge effects can be neglected in a first-order approximation, localized charge accumulation may also influence the sensing process. For instance, a number of works have reported the existence of electrostatic barriers that prevent the detection of low-energy particles and the release of photoelectrons from a spacecraft

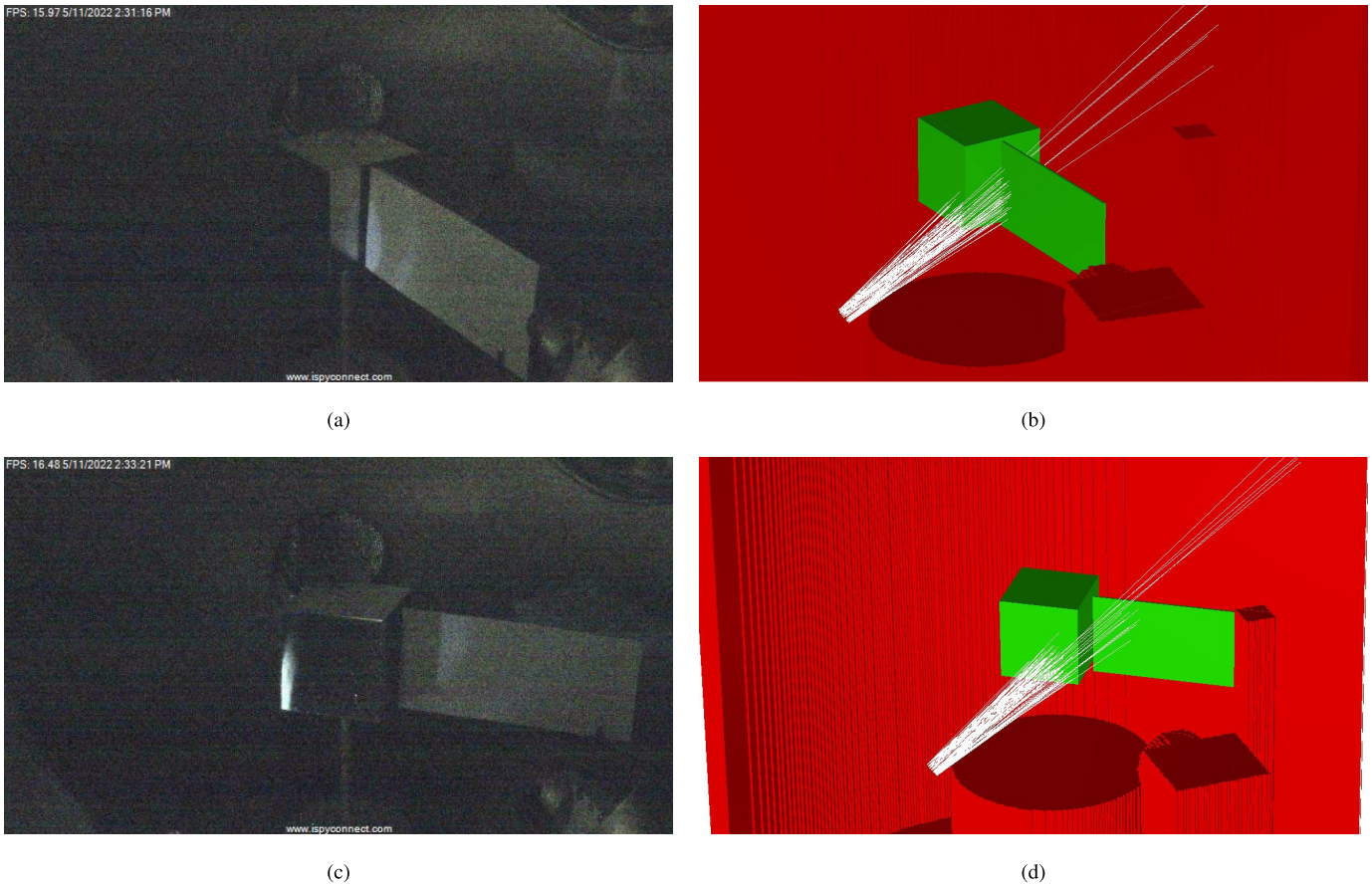

Fig. 4. Calibration of the position and heading of the UV light. (a) Experiment (30°). (b) SIMION (30°). (c) Experiment (70°). (d) SIMION (70°).

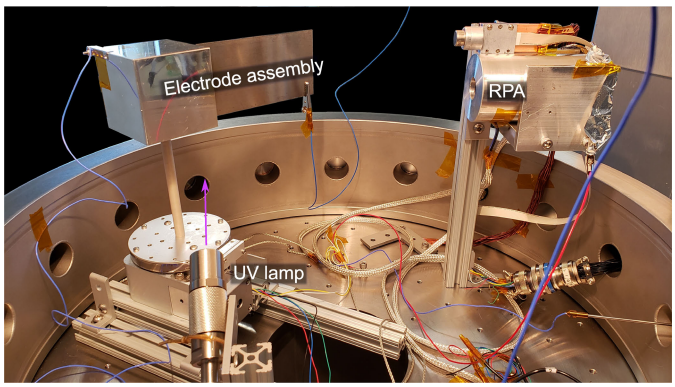

Fig. 5. Experimental setup.

surfaces [47], [48], [49], [50]. The effect is important near the Sun but becomes far less concerning for distances beyond 0.3 AU [49], [50]. As discussed in [5], well-focused high-current beams may lead to localized electrostatic barriers but, from a practical perspective, this should not significantly influence the trajectory of secondaries.

C. Experimental Setup

To assess the validity of the particle tracing framework presented in Section II-B, the experimental setup pictured in Fig. 5 is installed in the ECLIPS vacuum chamber [51]. Its geometrical configuration is almost identical to the one adopted in [5] and includes a spacecraft-like electrode assembly composed of a 70 × 70 × 70 mm^3 cube and a 145 × 60 mm^2 panel. The rotation of this structure is controlled by a stepper engine and monitored by an incremental rotary high-vacuum Renishaw Tonic encoder. The assembly is irradiated by a Hamamatsu L10706-S2D2 UV light source that excites the emission of photoelectrons, while a retarding potential analyzer (RPA) located at least 95 mm away from the tip of the panel measures the outgoing flux of photoelectrons. Their energy spectrum is recorded for different angles, unveiling the spatial flux distribution.

The electrode assembly is connected to a Matsusada AU-30R1 high-voltage power supply that imposes potentials between −100 and −900 V. The heading of the assembly spans from −40° to 100°, with 0° corresponding to a perfect alignment between the electron beam of the ECLIPS facility and the panel electrode. Although the electron beam is not used in this experiment, this reference point is kept consistent with the results presented in [5]. The RPA forms an angle of ∼16° with the electron beam axis.

III. Results

Prior to the discussion of the UV laser touchless potential sensing applications, the numerical model introduced in Section II-B is tested and validated using the vacuum chamber setup described in Section II-C.

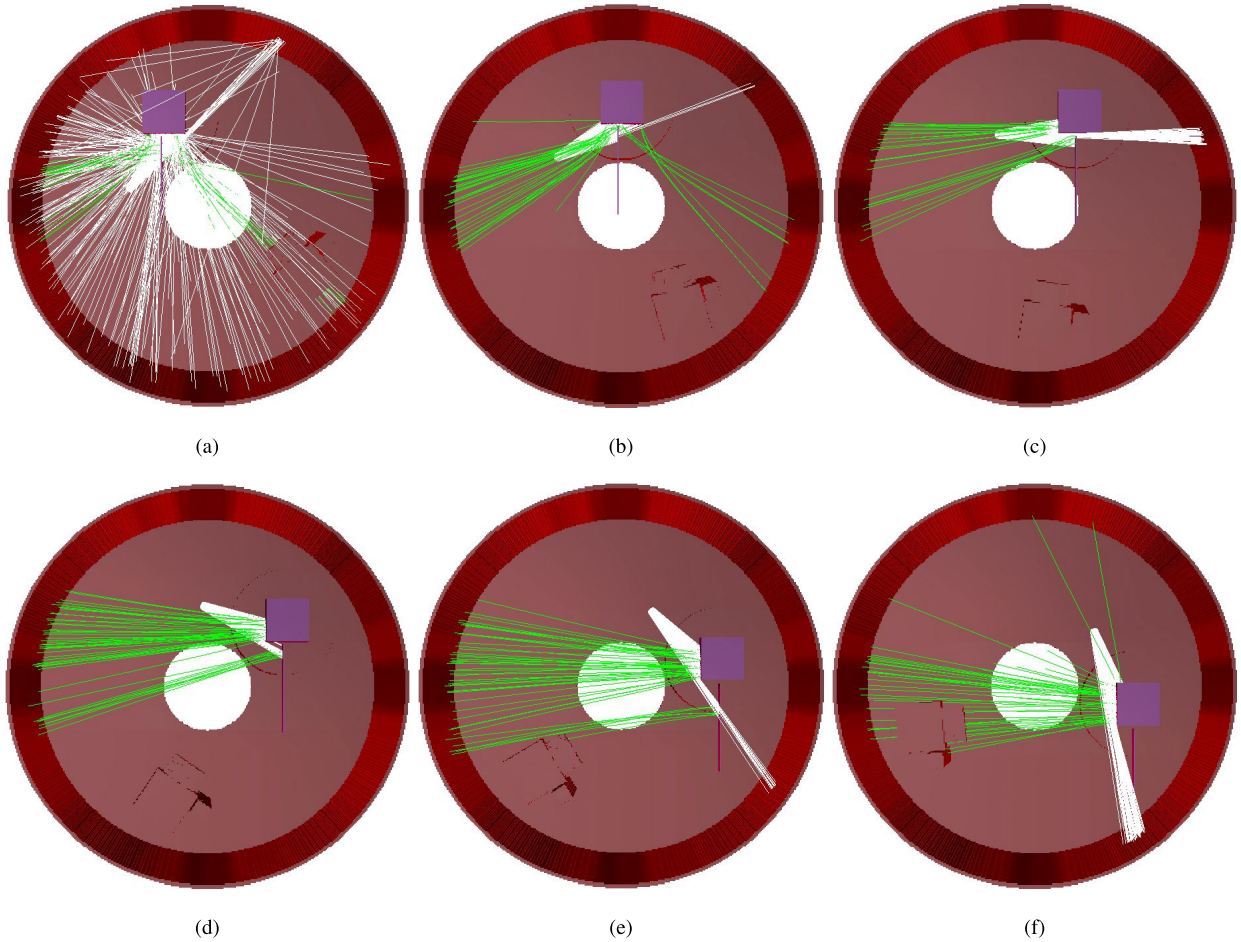

Fig. 6. Overview of photoelectron trajectories (green) generated by the UV source (white) as a function of the electrode assembly heading angle. The first iteration of reflected photons is shown for −25° and removed for clarity in the other cases. (a) −25°. (b) 0°. (c) 25°. (d) 50°. (e) 75°. (f) 100°.

A. Particle Trajectories

The trajectories of 500 randomly sampled photons are first propagated in Fig. 6 to characterize the flux of photoelectrons coming out of the electrode assembly. A single consecutive photon reflection is considered for −25° to illustrate this effect, but it is then removed from the other cases for clarity. The results obtained in this work are computed with an unlimited number of reflections. A brief study of the plots indicates that photolectrons will be detected between −25° and 0° and between 75° and 100°. Reflected photons may also induce photoemission, but this may be considered a second-order effect due to the large volume of the vacuum chamber.

B. Experimental Analysis

The potential of the electrode assembly described in Section II-C is set to −100 to −900 V with steps of −200 V while being irradiated by the UV source. The electrodes are rotated in steps of 2.5° while the electron signal is recorded. When detected, photoelectrons appear in the energy spectrum of the RPA as a prominent, isolated peak. Instead of measuring the full energy spectrum, the RPA records the photoelectron current 50 eV below the electrode potential and subtracts it from the measurement taken 50 eV above. This value represents the RPA current generated by photoelectrons with energies in the ±50-eV band around the potential of the electrode assembly. In this way, the geometrical distribution of the photoelectron flux is characterized with minimum time consumption.

Fig. 7 shows comparison of the experimental results with numerical simulations performed in SIMION with and without diffuse photon reflections. In both the cases, the model is able to identify the angles for which the photoelectron flux is detected, the overall trend with the applied electrode potential, and the order of magnitude of the signal. The most prominent difference with the experimental results is observed in the peak between 75° and 100°, which is overestimated by one order of magnitude in the simulations. Fig. 6 shows that this rotation corresponds to photon incidence angles close to 90°. Those fall beyond the validity range of (2), which heavily overestimates the photoelectron yield in this regime [34]. In other words, the simplified models presented in Section II-A do not provide a good representation of the photoelectric effect at high incidence angles. However, this is not a critical concern for the technical applications presented in this article, where the UV source and the detector are located on the same spacecraft and incidence angles close to the normal are expected.

The elimination of photon reflections results in a qualitatively better agreement with the experiments, particularly around −30° and 60°. The small divergence induced by the

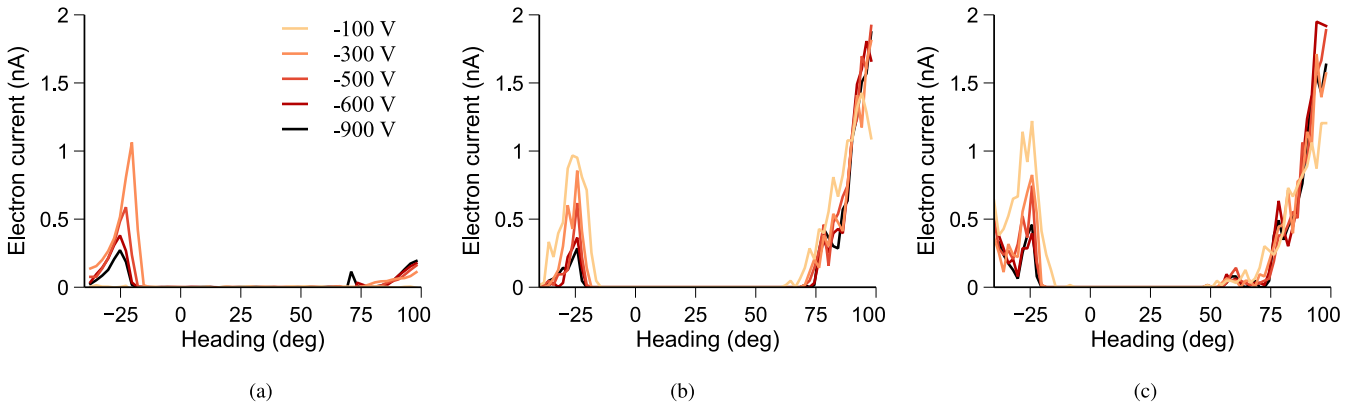

Fig. 7. Comparison of the experimental and simulated currents from the electrode assembly as a function of its potential and heading angle. The currents correspond to the electron flux entering the RPA in the ±50-eV band around the electrode potential. (a) Experiment. (b) SIMION, no photon reflections. (c) SIMION, diffuse photon reflections.

inclusion of diffuse reflections, besides unexpected, is also indicative of small geometrical modeling errors. From a technical perspective, however, the similarity between both the results supports the use of computationally efficient models without particle reflections in spacecraft charging applications.

A final interesting feature is the photoelectric current decrease with the applied electrode potential for a −25° heading angle. As observed in Fig. 6, the panel of the assembly acts in this case as an electrostatic deflector: when the potential decreases, the flux progressively moves away from the RPA and the signal is lost. Similar effects should be expected in future space applications and need to be accounted for using on-board particle tracing algorithms.

IV. Discussion

The results presented in Section III show that particle tracing simulations using simplified models can be used to compute the detectability of a target spacecraft and an order of magnitude estimate of the photoelectron fluxes when irradiated with a UV source. This opens the possibility of replacing low-energy electron beams by high-energy UV lasers for secondary electron generation. Some of the applications enabled by this new approach are subsequently discussed.

A. Touchless Potential Sensing

Active photoelectron-based sensing makes use of UV lasers mounted on a servicer to release low-energy photoelectrons from a target. After being accelerated by the electrostatic environment, photoelectrons reach the servicer with an energy that is approximately equal to the potential difference between the crafts. The flux is characterized by an RPA which determines the energy of incoming electrons. Knowing the potential of the servicer by means of, e.g., Langmuir probes, that of the target is finally computed.

UV lasers pass a long-wavelength laser through nonlinear crystals, which reduce the wavelength to the desired value. Tunable and fixed-wavelength technologies are used in Raman spectroscopy, photoemission spectroscopy, or photoluminscence, among others [52]. Commercial-off-the-shelf (COTS) lasers are already available for this purpose, with a nonexhaustive sample of them being listed in Table I. Furthermore, laser systems have been implemented and proposed for several spacecraft applications. For example, the GRACE-FO mission uses a laser ranging interferometer with a wavelength of 1064 nm to consistently determine the separation distance between the leader–follower formation [53]. In addition, high output power (several kW) space-based lasers have been proposed to ablate and induce a kinetic impulse on target debris, altering its trajectory such that it deorbits [54], [55], [56]. The background work on these systems will likely ease the implementation of UV lasers for touchless potential sensing.

TABLE I
Representative Parameters of COTS UV Lasers

Model	Divergence (mrad)	λ (nm)	$\overline{\omega}$ (eV)	P_{ph} (mW)
TOPTICA Photonics CW213	1	190	6.5	20
Photon Systems HeAg-224SL	4	224.3	5.5	50
Opto Engine LLC MPL-N-257	1	257	4.8	15
Photon Systems NeCu 30-248	4	248	5	50

The photoelectron current must be stronger than the background plasma environment to ensure that its signal is detected by the RPA. The spacecraft charging scenario studied in [19] is subsequently adopted to assess the feasibility of this process. Two generic spacecraft representing a servicer (GOESR, 0 V) and a target (SSL1300, −2.5 kV) are simulated in MATLAB with 30 m of separation. Photoelectrons are then generated from a point on the target solar panel with energies of 1 eV and a Lambertian emission distribution, and their trajectories are propagated as they approach the target under the influence of the electrostatic environment approximated with the multi-spheres method (MSM) [19], [57], [58].

Photoelectrons are displayed in Fig. 8 as they get closer to the target. The area covered by the photoelectron flux at the servicer, A_{final}, is estimated from the average radius of the cross section in the xy plane, resulting in 2.42 m^2. Such a large area indicates that the system will be robust to small pointing errors of the UV laser or an imperfect characterization of the electrostatic environment. Furthermore, the MSM does not

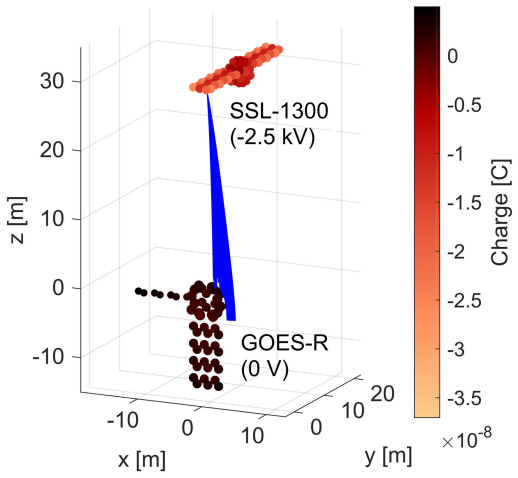

Fig. 8. Photoelectron trajectories (blue) from a target (SSL1300, −2.5 kV) as they approach the servicer (GOESR, 0 V). The charge distribution and photoelectron trajectories are determined using the MSM [19].

include space charge effects, or expansion of the photoelectron trajectories due to repulsion between the electrons. As a result, the final area may be larger, improving the robustness of the system to errors. For an initial emission current $I_{\mathrm{UV},0}$, the sensed current is found as follows:

$$I_{\mathrm{UV,sensed}} = I_{\mathrm{UV},0}\frac{A_{\mathrm{det}}}{A_{\mathrm{final}}} \tag{19}$$

where A_{det} is the area of the detector. For an initial current of 250 nA, or approximately equal to the current induced by the TOPTICA Photonics CW213 laser listed in Table I, and a 2-cm radius RPA, the measured current is 0.13 nA. The incident electron current flux to an uncharged spherical spacecraft as a function of the electron velocity distribution in a Maxwellian plasma can be found as [2]:

$$I(E_2) - I(E_1) = \frac{q_e n_e A}{(2\pi m_e)^{1/2}(k_B T_e)^{3/2}} \int_{E_1}^{E_2} e^{-E/k_B T_e} E \mathrm{d}E \tag{20}$$

where A is the area of the sensor, m_e is the mass of an electron, and E is the electron energy, or $E = (1/2)m_e v_e^2$, assuming nonrelativistic particles. The current is modeled for the worst case GEO environment with the parameters listed in Table II. RPAs can filter between particles of different energies, allowing the electron spectrum to be captured. The energy resolution $\Delta E/E$ characterizes the detector and is chosen to be 8% for this study based on [8] and [59]. The current measured as a function of energy is shown in Fig. 9. The bin that contains the photoelectron current emitted from the target (2.5 kV) is approximately an order of magnitude larger than the neighboring bins, indicating that photoelectron-based touchless potential sensing is feasible even in worst case GEO space weather conditions. In addition, the UV laser is not susceptible to perturbations due to the electrostatic environment, so photoelectron emissions may be excited at larger distances than possible with an electron gun even though the detected current decreases with increasing separation distance [8]. The magnetic field orientation may

TABLE II
GEO ENVIRONMENT PARAMETERS ADOPTED IN THE INVESTIGATION

Parameter	Kp=0	Kp=6	Worst Case
Electron number density (m^{-3})	7.5E5	10E5	30E5
Ion number density (m^{-3})	7.5E5	8E5	30E5
Electron Temperature (eV)	800	2200	12000
Ion Temperature (eV)	7600	8500	30000

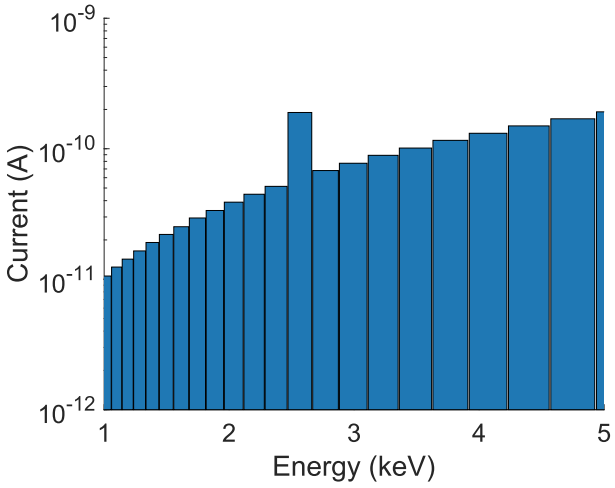

Fig. 9. Model of RPA signal for touchless potential sensing using UV-laser-induced photoelectrons assuming an instrument resolution of 8%.

also be taken advantage of to guide emissions over distances comparable to the electron gyroradius, as it has been shown that aligning the servicer and the target along the same field line may allow electron emission measurements as far as 1 km away [29]. If needed, an instrument with higher resolution or a collimator may be used to enhance the signal-to-noise ratio of the detector [60].

The active photoemission approach can be used alone or in combination with high-energy electron beams. However, the standalone implementation risks increasing the target potential by releasing photoelectrons, eventually preventing their emission [61], [62] and inducing measurement errors. If the surface material is a dielectric or near a dielectric, it is possible for a potential barrier to form in which the more negative dielectric areas repel the photoelectrons back toward the more positive portion of the spacecraft being impacted by the UV laser [2]. To account for this, control algorithms may be implemented such that the servicer can aim the UV laser at portions of the spacecraft in which electron emissions are detectable. Because it is generally recommended that the use of dielectrics is minimized and surfaces are electrically connected in GEO space to avoid dangerous arc discharges [63], blocking of photoelectron emissions due to dielectrics should be minimal in GEO space. In addition, a concentrated laser beam may locally charge the target and shift its potential. A tradeoff study between laser power (i.e., active charging) and RPA sensitivity should be carried out in each application to identify the best operational

regime. To shed light on this problem, the next section explores the effect of the UV laser on the target object potential.

Photoelectron emissions may also, in theory, be used to determine the surface material on a target. Multiple lasers with energies between 2 and 10 eV could be used to sequentially excite the surface. The energy of the photon must exceed the work function of the material to excite photoemissions. Therefore, the minimum energy that produces a peak in the energy spectrum would become the closest approximation of the work function of the material, providing insight into probable surface materials. Although this application is very speculative at the time of writing, it may be worth exploring in future systems.

B. Charge Variation

The change in the floating potential of spherical spacecraft in eclipse GEO environments when UV lasers are used to excite photoemissions is determined. Three GEO eclipse environments are implemented: Kp = 0, Kp = 6, and the worst case GEO environment from the design specifications for natural environments (DSNEs) [64], [65]. The Kp index is a measurement of the horizontal displacement of the magnetic field, and as a result is a proxy of geomagnetic activity [64]. The environment parameters are presented in Table II.

The current balance equation in eclipse is [2]

$$I_e(V) - I_i(V) - I_s(V) - I_b(V) - I_{\text{ph}}(V) = 0 \tag{21}$$

where I_e is the incident electron current, I_i is the incident ion current, I_s is the secondary electron current, I_b is the backscattered electron current, and I_{ph} is UV laser photoelectron current. The orbit motion limited (OML) equations for spherical current collection are used, and the incident electron current is [2]

$$I_e = \frac{1}{4} q_e n_e v_e A \exp\left(\frac{q_e V}{k_B T_e}\right), \quad \text{for } V < 0 \tag{22a}$$

$$I_e = \frac{1}{4} q_e n_e v_e A \left(1 + \frac{q_e V}{k_B T_e}\right), \quad \text{for } V > 0 \tag{22b}$$

where A is the total surface area of the spacecraft, and v_e is the electron thermal velocity

$$v_e = \sqrt{\frac{2 k_B T_e}{m_e}}. \tag{23}$$

The incident ion current is

$$I_i = \frac{1}{4} q_e n_i v_i A \left(1 - \frac{q_e V}{k_B T_i}\right), \quad \text{for } V < 0 \tag{24a}$$

$$I_i = \frac{1}{4} q_e n_i v_i A \exp\left(\frac{-q_e V}{k_B T_i}\right), \quad \text{for } V > 0. \tag{24b}$$

The photoelectron current induced by a UV laser with photon flux n_{ph} [see (13)] is

$$I_{\text{ph}} = q_e Y(\omega, R) n_{\text{ph}}. \tag{25}$$

It should be noted that for a positively charged spacecraft, the photoelectrons may not have sufficient energy to overcome the electrostatic barrier. The emissions will be attracted back to the spacecraft, canceling the emitted current. Therefore, photoelectron current for a positively charged spacecraft is

$$I_{\text{ph}} = q_e Y(\omega, R) n_{\text{ph}} \exp\left(\frac{-q_e V}{k_B T_{\text{ph}}}\right), \quad \text{for } V > 0. \tag{26}$$

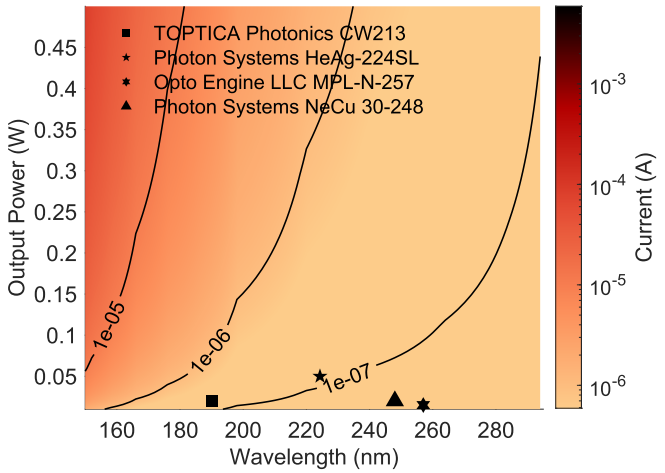

Fig. 10. Photoelectron current as a function of UV laser energy wavelength and output power. COTS UV lasers listed in Table I are scattered for comparison.

The photoelectron current induced by UV lasers as a function of output power and energy wavelength is shown in Fig. 10. The COTS lasers described in Table I are scattered on the figure as well, and their induced currents in aluminum targets range from 17 to 261 nA.

The backscatter and secondary electron yield are described in [5], [28], [29], and [30]. The electron incidence angle for the secondary and backscatter electron yield is again assumed to be 0°, and the combined secondary and backscatter yield is set as $\alpha = \eta + \delta$. To find α in a Maxwellian plasma, the yield is integrated over the distribution function

$$\alpha = \int_0^\infty (\eta(E) + \delta(E)) f_E(E) \tag{27}$$

where $f_E(E)$ is the Maxwellian energy distribution function

$$f_E(E) = \frac{2E^{1/2}}{\pi^{1/2}(k_B T_e)^{3/2}} \exp\left(\frac{-E}{k_B T_e}\right). \tag{28}$$

Using these emission yields, the final current balance equation is

$$I_e(V)(1 - \alpha) - I_i(V) - I_{\text{ph}}(V) = 0. \tag{29}$$

To assess the effects of the UV laser on a series of spherical objects with 0.25-, 0.5-, and 0.75-m radius in eclipse, Fig. 11 provides the potential increase as a function of the UV laser wavelength and output power. The color scale is different for each environment because the floating potential achieved in the absence of the UV laser photoelectron current is different, as indicated in the subcaptions. Higher potential differences (black surfaces) indicate that the spacecraft has been brought to a slightly positive potential due to the UV laser photoelectron current. As the radius increases, the UV laser energy and power required to bring the target spacecraft

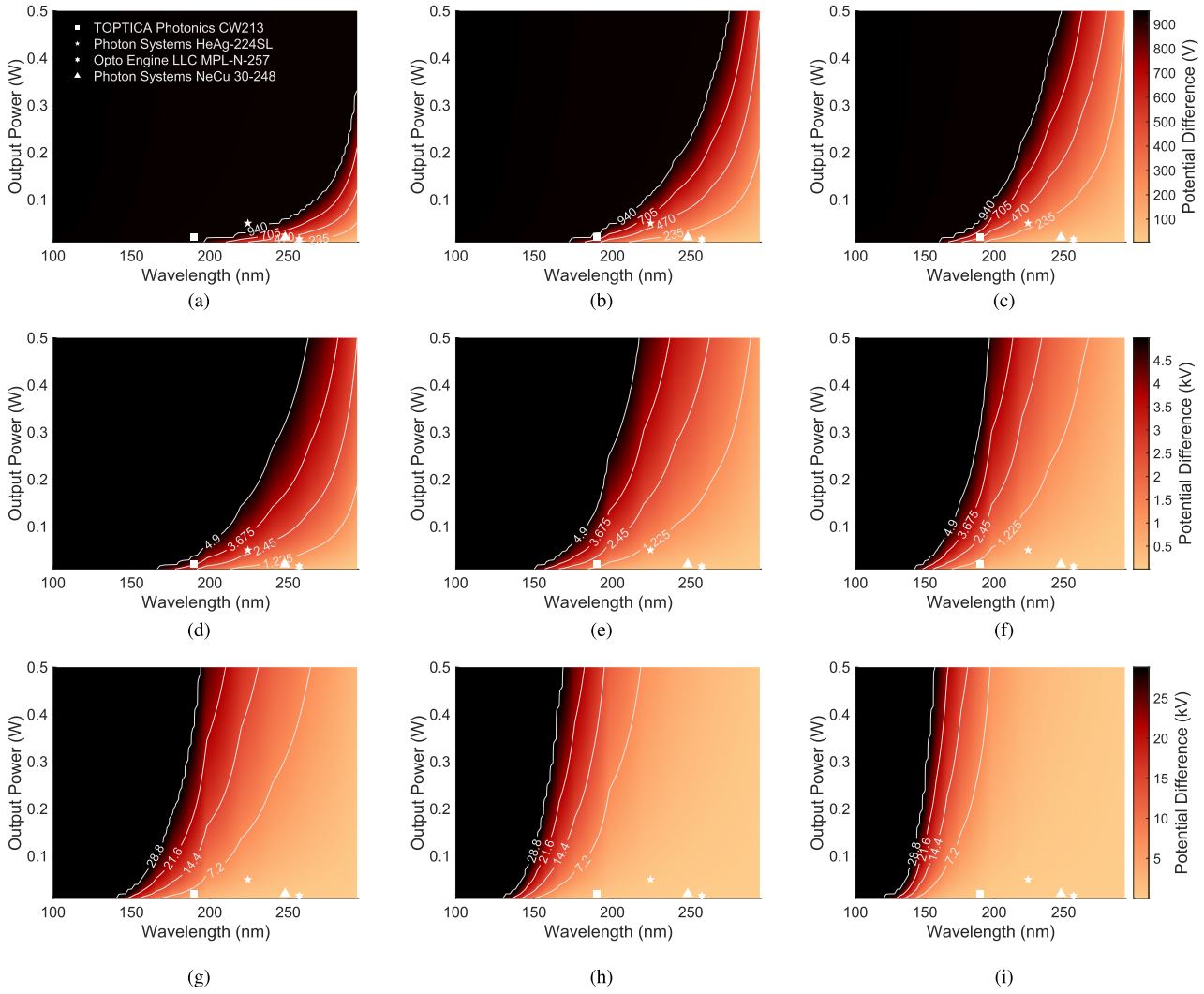

Fig. 11. Change in floating potential of a 0.25-, 0.5-, and 0.75-m radius spherical spacecraft in various GEO eclipse environments as a function of UV laser energy wavelength and output power. COTS UV lasers listed in Table I are scattered for comparison. (a) 0.25-m radius, Kp = 0, $V_{\mathrm{fl}} = -943.96$ V. (b) 0.5-m radius, Kp = 0, $V_{\mathrm{fl}} = -943.96$ V. (c) 0.75-m radius, Kp = 0, $V_{\mathrm{fl}} = -943.96$ V. (d) 0.25-m radius, Kp = 6, $V_{\mathrm{fl}} = -4,975.12$ V. (e) 0.5-m radius, Kp = 6, $V_{\mathrm{fl}} = -4,975.12$ V. (f) 0.75-m radius, Kp = 6, $V_{\mathrm{fl}} = -4,975.12$ V. (g) 0.25-m radius, worst case, $V_{\mathrm{fl}} = -28,856$ V. (h) 0.5-m radius, worst case, $V_{\mathrm{fl}} = -28,856$ V. (i) 0.75-m radius, worst case, $V_{\mathrm{fl}} = -28,856$ V.

to a positive potential increases as well. This occurs because the current from sources other than the UV laser increase in magnitude with increasing radius. However, the photoelectron current induced by the UV laser remains invariant with the target radius. The operational points of the COTS UV lasers listed in Table I are scattered over the results using white markers. As the environmental conditions become more extreme and the spacecraft floats to a more negative potential, more powerful and energetic lasers are required to bring the spacecraft to a positive potential. However, if the desired application of the UV laser is to excite photoelectrons for touchless potential sensing without altering the target spacecraft potential, more extreme conditions are favorable. Therefore, the ambient environmental conditions and desired application must be considered when selecting a UV laser. In general, the laser's output power and wavelength should be maximized to minimize the target's potential, and the laser's wavelength and output power should be minimized to touchlessly sense the target's potential without altering it.

C. Inclusion of Energetic Electron Beams

The operational conditions for the X-ray method, described in [6] and [7], are the exact opposite of the secondary electron method. The emission of X-rays is enhanced for high-energy primary electron impacts, while the emission of secondary electrons is (generally) minimized [6], [27]. The higher electron velocity also increases its gyroradius, leading to quasi-rectilinear (hence, easily predictable) trajectories. Finally, the backscattered electron yield remains relatively constant with surface degradation, as shown in Fig. 12.

Although the X-ray sensing method is particularly robust to target rotations [7], it is significantly less accurate than the electron method [26], which in turn becomes highly dependent on the electrostatic environment [5]. Both the approaches are therefore complementary but hard to implement with the same electron beam because they operate at different energetic regimes. It is in this context that high-energy UV lasers become a technically attractive alternative to low-energy electron beams for electron generation.

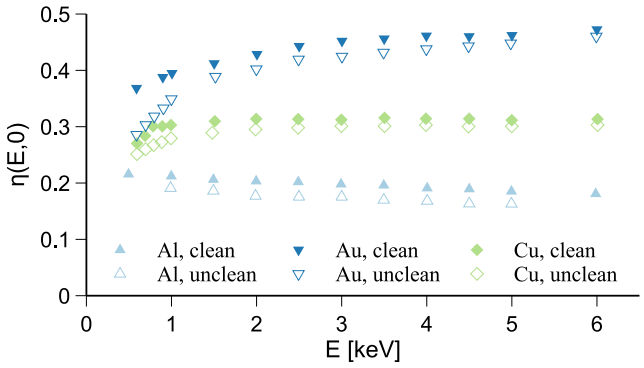

Fig. 12. Backscattered electron yield for selected materials as a function of the impacting electron energy [44].

Photons are insensitive to the electrostatic environment and involve additional advantages at high energies, such as stable photoelectric yield $Y[\omega, R]$ with surface contamination [43] and reduced reflectance $R(\omega, \phi, \sigma)$ (see Fig. 14). Therefore, the combined use of high-energy electron beams and lasers can result in significant benefits in terms of robustness, accuracy, and uncertainty mitigation by decoupling the photoelectron and X-ray generation processes.

D. Neutral Charging

The decoupling of the X-ray and secondary electron generation processes and the net negative and positive current fluxes that they, respectively, impart on the target brings the opportunity of measuring the target potential without significantly altering the measurement, referred to here as neutrally charging the target. To do so, the positive and negative current fluxes must be balanced.

The photoelectron current induced by a UV laser has been derived in (25). Similarly, the current imparted by high-energy electrons after neglecting secondary electron generation is [2]

$$I_e \approx [1 - \eta(Z, \phi)] I_b \tag{30}$$

where I_b is the current of the electron beam. The assumption $\delta(E, \phi) \ll \eta(Z, E, \phi)$ holds for beam energies E_b of the order of 10 s of keV and for most materials.

If follow-up interactions produced by backscattered electrons and reflected photons are ignored, the condition for neutral charging is obtained by equaling (25) and (30), resulting in

$$I_b = \frac{q_e}{\overline{\omega}} \frac{Y(\omega, R)}{[1 - \eta(Z, 0, \phi)]} P_{\text{ph}} \tag{31}$$

which gives the electron beam current I_b required to balance, in first-order approximation, the charge induced by a laser with power P_{ph} and photon energy ω for $E_b \gg 1$ keV. If the target material is known, good estimations of the surface properties can be obtained using high-energy electron beams and lasers. However, simulation frameworks like the one introduced in Section II-B are needed to account for backscattered electrons, reflected photons, and, for materials with high yields at high impact energies (e.g., gold), secondary electrons. The exact same approach could be used in combination with the spacecraft charging model presented in Section IV-B to set the target potential to a certain value, space weather permitting, and determine the stability of the solution.

V. Conclusion

UV lasers are revealed as a feasible method for photoelectron-based touchless spacecraft potential sensing and control in GEO and deep space. The currents generated by this approach on a typical servicer–target scenario are measurable in worst case space weather conditions and can be used to mitigate spacecraft charging in cold plasma. In more active environments and for larger spacecraft, the photoelectric current has a minor effect on the equilibrium potential, making it less dependent on the sensing process. The validation of a simplified modeling framework shows that a first-order approximation to the problem is sufficient to determine the detectability and order of magnitude of the photoelectron flux. Ultimately, this computationally efficient particle tracing model may find application in closed-loop potential sensing strategies and on-ground studies.

The use of UV lasers overcomes the technical challenges of previous electron-based sensing methods by minimizing or eliminating multiple sources of uncertainty, in particular, the effect of the electrostatic environment on low-energy electron beams and the degradation induced by surface contamination. The additional consideration of energetic electron beams can potentially enhance the robustness and accuracy of the sensing method while enabling novel charge control strategies (i.e., neutral sensing).

Appendix A
Electrostatic Framework

As a reference to the reader, the basic assumptions of the electrostatic framework implemented in Section II-B are subsequently described. Further details on this topic and the modeling of secondary electrons can be consulted in [5].

A. Maxwell Equations

The touchless potential sensing problem is characterized in GEO by quasi-static magnetic fields in the absence of electrically polarizable media. The electromagnetic environment is, consequently, modeled through the simplified Gauss and Faraday equations

$$\nabla \cdot \boldsymbol{E} = \frac{\rho_v}{\epsilon_0} \tag{32a}$$

$$\nabla \times \boldsymbol{E} = 0 \tag{32b}$$

where $\boldsymbol{E}$ is the electric field, ρ_v is the free charge density, and ϵ_0 is the permittivity of vacuum. As a consequence of (32b), the electric field derives from the electrostatic potential V through

$$\boldsymbol{E} = \nabla V. \tag{33}$$

In addition, it is useful to note that the integral form of (32b) leads to $\boldsymbol{E}$ being normal to the interface between a conductor (for which $\boldsymbol{E} = 0$) and free space [29].

The free charge density ρ_v is zero in a neutral plasma, but the presence of a charged spacecraft disrupts this equilibrium state and generates a charge distribution around the body. Still, for the low-density (0.1–1 particles per cm^{-3}) GEO environment, the effect of ρ_v is usually negligible at distances of tens of meters and $\rho_v \approx 0$ can be safely assumed (see Section II-B6). Under this condition, (32a) reduces to Laplace's equation

$$\nabla^2 V = 0 \tag{34}$$

which features significant computational advantages when solved in combination with the Dirichlet or Neumann boundary conditions for V.

B. Particle Dynamics

The relativistic change in momentum of a charged particle in a predefined electromagnetic environment is given by the balance

$$\frac{\mathrm{d}(\gamma m \boldsymbol{v})}{\mathrm{d}t} = \boldsymbol{F} \tag{35}$$

with $\boldsymbol{F}$ denoting the Lorentz force

$$\boldsymbol{F} = q(\boldsymbol{v} \times \boldsymbol{B} + \boldsymbol{E}) \tag{36}$$

and where $\boldsymbol{v}$, q, and m are the particle velocity, charge, and mass, respectively, $\gamma = (1 - \beta^2)^{-1/2}$ is the Lorentz factor, $\beta = v/c$, c is the speed of light, $\boldsymbol{B}$ is the magnetic flux density, t is the time, and an inertial time derivative is considered. It should be noted that in accordance with the special theory of relativity, the inertia of a particle with respect to a reference frame depends on its speed with respect to such frame. Consequently, the term γm defines the apparent mass of the particle. The position $\boldsymbol{x}$ in the inertial reference frame can be computed by integrating

$$\frac{\mathrm{d}\boldsymbol{x}}{\mathrm{d}t} = \boldsymbol{v}. \tag{37}$$

APPENDIX B
MATERIAL PROPERTIES

The secondary electron, X-ray, and photoelectron emission processes depend on a series of surface properties that must be characterized in a laboratory environment. Although the experiments performed in this work use aluminum targets, this section presents literature values for a range of space materials as a reference.

A. Secondary Electron Emission

The parameters $\delta_{\max}$ and $E_{\max}$ define the shape of the Sanders and Inouye secondary electron yield curve and its angular dependence according to the Darlington and Cosslett model, while the work function φ of the conductive material determines the Chung–Everhart secondary electron energy distribution. The electron affinity χ defines the energy separation between the lowest possible state for any excited electron in a dielectric material and the vacuum level, and it may be used in place of the work function when analyzing dielectrics [66]. Table III reports these values together with the first (E_1) and second (E_2) crossover points (for which $\delta = 1$) for selected materials [66], [67].

TABLE III
EMISSION PARAMETERS FOR SELECTED MATERIALS [66], [67]

Material	Z	φ/χ [eV]	$\delta_{\max}$	$E_{\max}$ [eV]	E_1 [eV]	E_2 [eV]
Aluminum	13	4.20	1.0	300	300	300
Gold	79	5.47	1.4	800	150	>2000
Copper	29	5.10	1.3	600	200	1500
Iron	26	4.67	1.3	400	120	1400
Kapton	4.7	5.8	1.67	280	50	750
Teflon	3.8	4.1	2.4	350	50	180

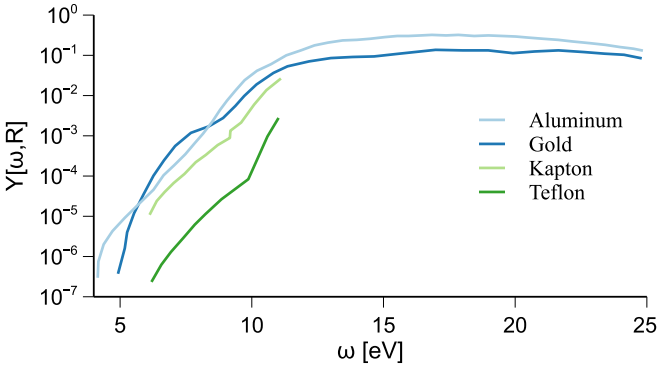

Fig. 13. Photoelectric yield for selected materials as a function of the impacting photon energy [43], [68], [69].

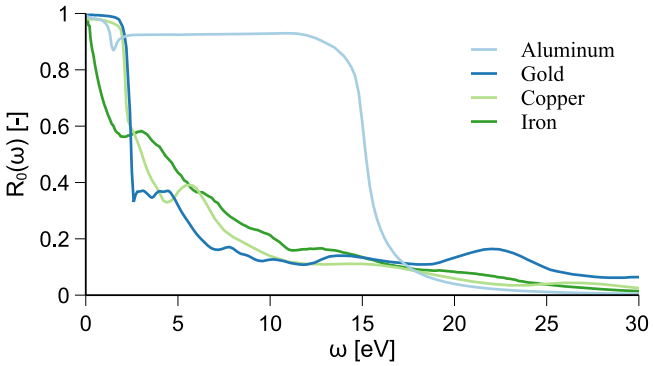

Fig. 14. Normal reflectance for selected materials as a function of the impacting photon energy [67], [69], [70].

B. Backscattered Electron Yield

Fig. 12 depicts the yield values below 6 keV for clean (ion bombarded) and unclean samples of aluminum, gold, and copper from [44]. As expected, clean and unclean values converge and the measurements stabilize as E grows. The backscattered electron yield can reach up to 50%, highlighting the importance of this effect for some materials. In the experiments presented in this article, however, energetic electrons do not impact the electrode assembly and backscattered electrons are not considered.

C. Photoelectric Yield

The photoelectric yield $Y(\omega, 0)$ is usually characterized by means of well-controlled laboratory experiments. The results for aluminum, gold, Kapton, and Teflon are presented in Fig. 13 as a function of the photon impact energy. Kapton and Teflon are backed by silver [43]. In the case of aluminum

and gold, the yield increases with the impinging photon energy until it reaches a plateau at 10^{-1} and about 12 eV.

D. Normal Reflectance

Similar to the photoelectric yield, the normal reflectance of a perfectly smooth surface should be characterized experimentally. Fig. 14 shows the value of $R_0(\omega)$ for selected materials as a function of the impinging photon energy [67]. Kapton is backed by aluminum, as it would be on multilayer insulators [69], and Teflon is backed by silver. The reflectance decreases with the photon energy for all the materials, but aluminum remains highly reflective until ∼15 eV.

ACKNOWLEDGMENT

The authors thank Dr. Kieran Wilson for his comments on the article.

REFERENCES

[1] NASA. (2022). *NASA Strategic Plan*. [Online]. Available: https://www.nasa.gov/sites/default/files/atoms/files/fy_22_strategic_plan.pdf

[2] S. T. Lai, *Fundamentals of Spacecraft Charging: Spacecraft Interactions With Space Plasmas*. Princeton, NJ, USA: Princeton Univ. Press, 2012.

[3] R. C. Olsen, "Record charging events from applied technology satellite 6," *J. Spacecraft Rockets*, vol. 24, no. 4, pp. 362–366, 1987.

[4] M. T. Bengtson, K. T. Wilson, and H. Schaub, "Experimental results of electron method for remote spacecraft charge sensing," *Space Weather*, vol. 18, no. 3, pp. 1–12, Mar. 2020.

[5] A. Romero-Calvo, J. Hammerl, and H. Schaub, "Touchless potential sensing of differentially-charged spacecraft using secondary electrons," *J. Spacecraft Rockets*, vol. 59, no. 5, pp. 1623–1633, 2022.

[6] K. Wilson and H. Schaub, "X-ray spectroscopy for electrostatic potential and material determination of space objects," *IEEE Trans. Plasma Sci.*, vol. 47, no. 8, pp. 3858–3866, Aug. 2019.

[7] K. T. Wilson, M. T. Bengtson, and H. Schaub, "X-ray spectroscopic determination of electrostatic potential and material composition for spacecraft: Experimental results," *Space Weather*, vol. 18, no. 4, pp. 1–10, Apr. 2020.

[8] M. Bengtson, J. Hughes, and H. Schaub, "Prospects and challenges for touchless sensing of spacecraft electrostatic potential using electrons," *IEEE Trans. Plasma Sci.*, vol. 47, no. 8, pp. 3673–3681, Aug. 2019.

[9] K. Champion and H. Schaub, "Electrostatic potential shielding in representative cislunar regions," *IEEE Trans. Plasma Sci.*, early access, Jan. 25, 2023, doi: 10.1109/TPS.2023.3236246.

[10] K. Wilson and H. Schaub, "Impact of electrostatic perturbations on proximity operations in high Earth orbits," *J. Spacecraft Rockets*, vol. 58, no. 5, pp. 1293–1302, Sep. 2021.

[11] K. Wilson, A. Romero-Calvo, and H. Schaub, "Constrained guidance for spacecraft proximity operations under electrostatic perturbations," *J. Spacecraft Rockets*, vol. 59, no. 4, pp. 1304–1316, Jul./Aug. 2022.

[12] H. Schaub, G. G. Parker, and L. B. King, "Challenges and prospects of Coulomb spacecraft formation control," *J. Astron. Sci.*, vol. 52, nos. 1–2, pp. 169–193, Mar. 2004.

[13] F. Casale, H. Schaub, and J. D. Biggs, "Lyapunov optimal touchless electrostatic detumbling of space debris in GEO using a surface multisphere model," *J. Spacecraft Rockets*, vol. 58, no. 3, pp. 764–778, May 2021.

[14] H. Schaub and D. F. Moorer Jr., "Geosynchronous large debris reorbiter: Challenges and prospects," *J. Astron. Sci.*, vol. 59, nos. 1–2, pp. 161–176, 2012.

[15] J. Hughes and H. Schaub, "Prospects of using a pulsed electrostatic tractor with nominal geosynchronous conditions," *IEEE Trans. Plasma Sci.*, vol. 45, no. 8, pp. 1887–1897, Aug. 2017.

[16] M. Bengtson, K. Wilson, J. Hughes, and H. Schaub, "Survey of the electrostatic tractor research for reorbiting passive GEO space objects," *Astrodynamics*, vol. 2, no. 4, pp. 291–305, Dec. 2018.

[17] J. A. Hughes and H. Schaub, "Electrostatic tractor analysis using a measured flux model," *J. Spacecraft Rockets*, vol. 57, no. 2, pp. 207–216, Mar. 2020.

[18] J. Hammerl and H. Schaub, "Effects of electric potential uncertainty on electrostatic tractor relative motion control equilibria," *J. Spacecraft Rockets*, vol. 59, no. 2, pp. 552–562, Mar. 2022.

[19] Á. Romero-Calvo, G. Cano-Gómez, and H. Schaub, "Simulation and uncertainty quantification of electron beams in active spacecraft charging scenarios," *J. Spacecraft Rockets*, vol. 59, no. 3, pp. 739–750, May 2022.

[20] J. A. Reyes et al., "Spectroscopic behavior of various materials in a GEO simulated environment," *Acta Astronautica*, vol. 189, pp. 576–583, Dec. 2021.

[21] V. Baglin et al., "The secondary electron yield of technical materials and its variation with surface treatments," in *Proc. 7th Eur. Part. Accel. Conf.*, Vienna, Austria, 2000, pp. 217–221.

[22] S. Robertson, Z. Sternovsky, and B. Walch, "Reduction of asymmetry transport in the annular Penning trap," *Phys. Plasmas*, vol. 11, no. 5, pp. 1753–1756, May 2004.

[23] C. Jin, A. Ottaviano, and Y. Raitses, "Secondary electron emission yield from high aspect ratio carbon velvet surfaces," *J. Appl. Phys.*, vol. 122, no. 17, Nov. 2017, Art. no. 173301.

[24] M. F. Diaz-Aguado et al., "Experimental investigation of total photoemission yield from new satellite surface materials," *J. Spacecraft Rockets*, vol. 56, no. 1, pp. 248–258, Jan. 2019.

[25] P. Lundgreen, "The development and use of a secondary electron yield database for spacecraft charge modeling," Ph.D. dissertation, Dept. Phys., Utah State Univ., Logan, UT, USA, 2020. [Online]. Available: https://digitalcommons.usu.edu/etd/7929/

[26] K. Wilson, M. Bengtson, and H. Schaub, "Remote electrostatic potential sensing for proximity operations: Comparison and fusion of methods," *J. Spacecraft Rockets*, vol. 59, no. 5, pp. 1425–1436, Sep. 2022.

[27] R. E. Van Grieken and A. A. Markowicz, *Handbook of X-Ray Spectrometry*, 2nd ed. New York, NY, USA: Marcel Dekker, 2001.

[28] M. T. Bengtson and H. Schaub, "Electron-based touchless potential sensing of shape primitives and differentially-charged spacecraft," *J. Spacecraft Rockets*, vol. 58, no. 6, pp. 1847–1857, Nov. 2021.

[29] M. T. Bengtson, "Electron method for touchless electrostatic potential sensing of neighboring spacecraft," Ph.D. dissertation, Dept. Aerosp. Eng. Sci., Univ. Colorado Boulder, Boulder, CO, USA, 2020. [Online]. Available: http://hanspeterschaub.info/Papers/grads/MilesBengtson.pdf

[30] A. Romero-Calvo, K. Champion, and H. Schaub, "Touchless spacecraft potential sensing using energetic electron beams and active photoemission," in *Proc. Spacecraft Charging Technol. Conf.*, Apr. 2022.

[31] K. Wilson, J. Hammerl, and H. Schaub, "Using plasma-induced X-ray emission to estimate electrostatic potentials on nearby space objects," *J. Spacecraft Rockets*, vol. 59, no. 4, pp. 1402–1405, Jul. 2022.

[32] K. T. Wilson, "Remote electrostatic potential determination for spacecraft relative motion control," Ph.D. dissertation, Aerosp. Eng. Sci. Dept., Univ. Colorado, Boulder, CO, USA, 2021. [Online]. Available: http://hanspeterschaub.info/Papers/grads/KieranWilson.pdf

[33] J. Hammerl, Á. Romero-Calvo, A. Lopez, and H. Schaub, "Touchless potential sensing of complex differentially-charged shapes using X-rays," in *Proc. AIAA SCITECH Forum*, Jan. 2022, pp. 1–13.

[34] J. Jeanneret, "Photoemission in LHC—A simple model," Conseil Européen pour la Recherche Nucléaire (CERN), Geneva, Switzerland, Tech. Rep., 97–48, 1997. [Online]. Available: citeseerx.ist.psu.edu/viewdoc/download?doi=10.1.1.17.5847&rep=rep1&type=pdf

[35] C. J. Powell, "Analysis of optical- and inelastic-electron-scattering data. III. Reflectance data for beryllium, germanium, antimony, and bismuth," *J. Opt. Soc. Amer.*, vol. 60, no. 2, pp. 214–220, Feb. 1970.

[36] S. T. Lai and M. F. Tautz, "Aspects of spacecraft charging in sunlight," *IEEE Trans. Plasma Sci.*, vol. 34, no. 5, pp. 2053–2061, Oct. 2006.

[37] H. E. Bennett and J. O. Porteus, "Relation between surface roughness and specular reflectance at normal incidence," *J. Opt. Soc. Amer.* , vol. 51, no. 2, pp. 123–129, 1961.

[38] H. Bruining, *Physics and Applications of Secondary Electron Emission*. New York, NY, USA: McGraw-Hil, 1954, ch. 7.

[39] J. Greenwood, "The correct and incorrect generation of a cosine distribution of scattered particles for Monte-Carlo modelling of vacuum systems," *Vacuum*, vol. 67, no. 2, pp. 217–222, Sep. 2002.

[40] S. T. Lai, "Charging of mirror surfaces in space," *J. Geophys. Res.: Space Phys.*, vol. 110, no. 1, pp. 1–11, 2005.

[41] Hamamatsu Photonics. (2014). *S2D2 L10706 VUV Light Source Datasheet*. [Online]. Available: www.hamamatsu.com/content/dam/hamamatsu-photonics/sites/documents/99_SALES_LIBRARY/etd/L10706_TLSZ1001E.pdf

[42] M. S. Chung and T. E. Everhart, "Simple calculation of energy distribution of low-energy secondary electrons emitted from metals under electron bombardment," *J. Appl. Phys.*, vol. 45, no. 2, pp. 707–709, 1974.
[43] K. Kawasaki, S. Inoue, E. Ewang, K. Toyoda, and M. Cho, "Measurement of electron emission yield by electrons and photons for space aged material," in *Proc. 14th Spacecraft Charging Technol. Conf.*, Noordwijk, The Netherlands, 2016, pp. 1–7.
[44] A. Assa and M. El Gomati, "Backscattering coefficients for low energy electrons," *Scanning Microsc.*, vol. 12, no. 1, pp. 185–192, 1998.
[45] H. J. Fahr and M. Heyl, "Debye screening under non-equilibrium plasma conditions," *Astron. Astrophys.*, vol. 589, p. 85, May 2016.
[46] C. R. Seubert, L. A. Stiles, and H. Schaub, "Effective Coulomb force modeling for spacecraft in Earth orbit plasmas," *Adv. Space Res.*, vol. 54, no. 2, pp. 209–220, 2014.
[47] B. Thiébault, "Potential barrier in the electrostatic sheath around a magnetospheric spacecraft," *J. Geophys. Res.: Space Phys.*, vol. 109, no. 12, p. 12207, 2004.
[48] E. Engwall, A. I. Eriksson, and J. Forest, "Wake formation behind positively charged spacecraft in flowing tenuous plasmas," *Phys. Plasmas*, vol. 13, no. 6, Jun. 2006, Art. no. 062904.
[49] R. E. Ergun et al., "Spacecraft charging and ion wake formation in the near-sun environment," *Phys. Plasmas*, vol. 17, no. 7, Jul. 2010, Art. no. 072903.
[50] S. Guillemant, V. Génot, J.-C. Matéo-Vélez, P. Sarrailh, A. Hilgers, and P. Louarn, "Simulation study of spacecraft electrostatic sheath changes with the heliocentric distances from 0.044 to 1 AU," *IEEE Trans. Plasma Sci.*, vol. 41, no. 12, pp. 3338–3348, Dec. 2013.
[51] K. Wilson, Á. Romero-Calvo, M. Bengtson, J. Hammerl, J. Maxwell, and H. Schaub, "Development and characterization of the ECLIPS space environments simulation facility," *Acta Astronautica*, vol. 194, pp. 48–58, May 2022.
[52] S. Jin Zhang et al., "High power all solid state VUV lasers," *J. Electron Spectrosc. Rel. Phenomena*, vol. 196, pp. 20–23, Oct. 2014. [Online]. Available: www.sciencedirect.com/science/article/pii/S036820481400036X
[53] R. P. Kornfeld et al., "GRACE-FO: The gravity recovery and climate experiment follow-on mission," *J. Spacecraft Rockets*, vol. 56, no. 3, pp. 931–951, May 2019, doi: 10.2514/1.A34326.
[54] S. Shen, X. Jin, and C. Hao, "Cleaning space debris with a space-based laser system," *Chin. J. Aeronaut.*, vol. 27, no. 4, pp. 805–811, Aug. 2014.
[55] Q. Wen, L. Yang, S. Zhao, Y. Fang, Y. Wang, and R. Hou, "Impacts of orbital elements of space-based laser station on small scale space debris removal," *Optik*, vol. 154, pp. 83–92, Feb. 2018.
[56] C. R. Phipps and C. Bonnal, "A spaceborne, pulsed UV laser system for re-entering or nudging LEO debris, and re-orbiting GEO debris," *Acta Astronautica*, vol. 118, pp. 224–236, Jan. 2016. [Online]. Available: https://www.sciencedirect.com/science/article/pii/S0094576515300485
[57] D. Stevenson and H. Schaub, "Multi-sphere method for modeling spacecraft electrostatic forces and torques," *Adv. Space Res.*, vol. 51, no. 1, pp. 10–20, Jan. 2013.
[58] J. A. Hughes and H. Schaub, "Heterogeneous surface multisphere models using method of moments foundations," *J. Spacecraft Rockets*, vol. 56, no. 4, pp. 1259–1266, 2019.
[59] A. L. Victor, T. H. Zurbuchen, and A. D. Gallimore, "Top hat electrostatic analyzer for far-field electric propulsion plume diagnostics," *Rev. Sci. Instrum.*, vol. 77, no. 1, Jan. 2006, Art. no. 013505, doi: 10.1063/1.2165549.
[60] R. B. Torbert et al., "The electron drift instrument for MMS," *Space Sci. Rev.*, vol. 199, no. 1, pp. 283–305, Mar. 2016.
[61] R. C. Hoffmann, "Electron-induced electron yields of uncharged insulating material," Ph.D. dissertation, Phys. Dept., Utah State Univ., Logan, UT, USA, 2010.
[62] J. Christensen, "Electron yield measurements of high-yield, low-conductivity dielectric materials," Ph.D. dissertation, Dept. Phys., Utah State Univ., Logan, UT, USA, 2017.
[63] H. B. Garrett and A. C. Whittlesey, "Spacecraft design guidelines," in *Guide to Mitigating Spacecraft Charging Effects*. Hoboken, NJ, USA: Wiley, 2012, ch. 3, pp. 26–61.
[64] M. H. Denton, M. F. Thomsen, H. Korth, S. Lynch, J. C. Zhang, and M. W. Liemohn, "Bulk plasma properties at geosynchronous orbit," *J. Geophys. Res.: Space Phys.*, vol. 110, no. 7, pp. 1–17, 2005. [Online]. Available: https://agupubs.onlinelibrary.wiley.com/doi/abs/10.1029/2004JA010861
[65] F. B. Leahy, "Cross-program design specification for natural environments (DSNE)," Nat. Aeronaut. Space Admin., Washington, DC, USA, Tech. Rep. SLS-SPEC-159, 2021.
[66] L. Olano and I. Montero, "Energy spectra of secondary electrons in dielectric materials by charging analysis," *Results Phys.*, vol. 19, Dec. 2020, Art. no. 103456.
[67] D. R. Lide, *CRC Handbook of Chemistry and Physics*, 84th ed. Boca Raton, FL, USA: CRC Press, 2003.
[68] B. Feuerbacher and B. Fitton, "Experimental investigation of photoemission from satellite surface materials," *J. Appl. Phys.*, vol. 43, no. 4, pp. 1563–1572, 1972.
[69] H. Rodriguez, K. Abercromby, M. Mulrooney, and E. Barker, "Optical properties of multi-layered insulation," in *Proc. Adv. Maui Opt. Space Surveill. Technol. Conf.*, Maui, Hawaii, 2007.
[70] J. B. Heaney, "Evaluation of commercially supplied silver coated Teflon for spacecraft temperature control usage," NASA, Washington, DC, USA, Tech. Rep., TM-X-70488, 1974.

Álvaro Romero-Calvo is an Assistant Professor at the Daniel Guggenheim School of Aerospace Engineering, Georgia Institute of Technology, Atlanta, GA, USA. His laboratory develops space technologies for low-gravity environments, with a particular interest on low-gravity fluid mechanics, space charging, and the fundamental problems behind them. He has led the design of several microgravity experiments at ZARM's drop tower, Bremen, Germany, and Blue Origin's New Shepard, Kent, WA, USA. He has authored or coauthored 21 journal and 44 conference papers, as well as three patents.

Dr. Romero-Calvo is a member of the AIAA Microgravity and Space Processes Technical Committee. He currently serves as the Vice-Chair of the COSPAR Scientific Commission G and Board Member of ASGSR.

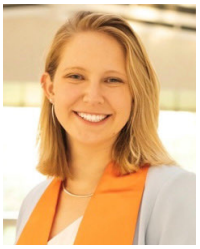

Kaylee Champion received the B.S. degree from Aerospace Engineering, The University of Texas at Austin, Austin, TX, USA, in 2021. She is currently pursuing the Ph.D. degree in astrodynamics with the Autonomous Vehicles Systems (AVS) Laboratory, University of Colorado at Boulder, Boulder, CO, USA.

She received the National Science Foundation Fellowship, in 2021, and the NSTGRO Fellowship, in 2022. Her current research interests include charged astrodynamics, spacecraft–plasma interactions, and mitigating space debris.

Hanspeter Schaub is a Professor and the Chair at the Aerospace Engineering Sciences Department, University of Colorado, Boulder, CO, USA. He holds the Schaden Leadership Chair. He has over 28 years of research experience, of which four years are at Sandia National Laboratories, Albuquerque, NM, USA. He has authored or coauthored 208 journal and 326 conference papers, as well as a fourth edition textbook on analytical mechanics of space systems. His research interests are in astrodynamics, relative motion dynamics, charged spacecraft motion, and spacecraft autonomy.

Dr. Schaub is a fellow of AIAA and AAS. He has been the ADCS Lead in the CICERO Mission, the ADCS Algorithm Lead on a Mars Mission, and Supporting ADCS for a new Asteroid Mission. In 2023, he won the Hazel Barnes Price, the top award granted to faculty at the University of Colorado. He has been awarded the H. Joseph Smead Faculty Fellowship, the Provost's Faculty Achievement Award, the faculty assembly award for excellence in teaching, and the Outstanding Faculty Advisor Award. He has won the AIAA/ASEE Atwood Educator award, AIAA Mechanics and Control of Flight award, and the Collegiate Educator of the Year for the AIAA Rocky Mountain Section.